Journal of Materials Science & Technology 155 (2023) 47–53

Contents lists available at ScienceDirect

Journal of Materials Science & Technology

journal homepage: www.elsevier.com/locate/jmst

Research Article

Ion diffusion, and hysteresis of magnesium hydride conversion electrode materials

Yingtong Lv[a,1], Xiang Zhang[a,1], Wei Chen[b], Shunlong Ju[b], Zhenhua Liu[a], Guanglin Xia[b], Takayuki Ichikawa[c], Tengfei Zhang[a,*], Xuebin Yu[b,*]

[a] Centre for Hydrogenergy, College of Materials Science and Technology, Nanjing University of Aeronautics and Astronautics, Nanjing 210016, China
[b] Department of Materials Science, Fudan University, Shanghai 200433, China
[c] Graduate School of Engineering, Hiroshima University, 739-8530 Higashi, Hiroshima, Japan

ARTICLE INFO

Article history:
Received 21 November 2022
Revised 30 December 2022
Accepted 11 January 2023
Available online 14 March 2023

Keywords:
Magnesium hydride
Lithium borohydrides
Graphene
Nano-crystallization
All-solid-state lithium-ion battery

ABSTRACT

MgH_2, owing to a high theoretical capacity of 2038 mAh g^{-1}, is regarded as a promising anode material for lithium-ion batteries (LIBs). However, the application of MgH_2 is still far from satisfactory due to its poor cycling stability. Herein, nano-crystallization of MgH_2 as an anode is applied for all-solid-state lithium-ion batteries (ASSLIBs) using $LiBH_4$ as a solid-state electrolyte. The self-assembly designed MgH_2 electrode on graphene could effectively alleviate the volume expansion, prevent the agglomeration of active substances, improve the electron transfer, and enhance the electrochemical performance of the anode material. As a result, a reversible capacity of 1214 mAh g^{-1} after 50 cycles is obtained. Significantly enhanced cycle life with a notable capacity of 597 mAh g^{-1} at a current density of 400 mA g^{-1} is delivered after 200 cycles. Further investigation on full cells also exhibits great application potential on ASSLIBs.

1. Introduction

In the field of energy storage and conversion, lithium-ion batteries (LIBs) are widely used in portable electronic devices, electric vehicles, and renewable energy storage systems due to their good cycle life and high energy density [1–3]. The specific energy density of LIBs as power sources, however, is only 200–300 Wh kg^{-1}, which is much lower than that of gasoline, 12,000 Wh kg^{-1}. Consequently, intensive research into electrode materials has been applied to improve their electrochemical performance [4–9]. Recently, potential candidates, such as carbides [10–14], hydrides [15–20], Si-based materials [21–25], sulfides [26–28], phosphides [29,30], and transition-metal oxides [31–33], niobium-based materials [34,35], and vanadium-based materials [36,37] have been deeply investigated as anode materials. Among them, metal hydrides have always been considered hydrogen storage materials [38–43]. From the myriad of available materials, Oumellal et al. [16] conceptually proposed that metal hydrides could be used as negative electrodes, based on the conversion reaction with lithium ions ($MH_x + xLi^+ + xe^- \rightleftharpoons M + xLiH$). Among various proposed metal hydrides, Mg hydride (MgH_2) has attracted great attention due to its high theoretical gravimetric (2038 mAh g^{-1}) and volumetric capacity (2878 mAh L^{-1}), as well as a low and safe potential window with an average voltage of 0.5 V versus Li^+/Li. However, this conversion reaction is accompanied by inevitable volume expansion or shrinkage, which limits the application of MgH_2 in LIBs. The capacity rapidly fades from 2036 mAh g^{-1} in the first cycle to 321 mAh g^{-1} after only 20 cycles (Figs. S1 and S2 in the Supporting Information).

To address these issues, various endeavors have been made to improve the performance of MgH_2 electrodes [44–48]. Inspired by recent research on silicon anodes, nanostructured materials can provide a larger specific surface area and a shorter distance of lithium mass diffusion and charge transport [2,49], resulting in enhanced cycling performance and storage capacity [50–54]. Bottom-up preparation of MgH_2 nanoparticles, achieved by Oumellal et al. [55], can alleviate the pulverization of bulk MgH_2 particles upon cycling. Even so, a capacity still decayed rapidly due to MgH_2 agglomeration. More recently, we have fabricated MgH_2 nanoparticles on graphene and conductive polymer, respectively. With this dispersion, a capacity of 395 mAh g^{-1} was obtained at a high current density of 2000 mA g^{-1} even after 1000 cycles [56]. According to the two-dimensional conductive network, the MgH_2 electrode delivers a high reversible specific capacity of 1311 mAh g^{-1} at 100 mA g^{-1} and an excellent rate performance of 1025 mAh g^{-1}

* Corresponding authors.
E-mail addresses: zhangtengfei@nuaa.edu.cn (T. Zhang), yuxuebin@fudan.edu.cn (X. Yu).
[1] These authors contributed equally to this work.

https://doi.org/10.1016/j.jmst.2023.01.028
1005-0302/

at 2000 mA g^{-1} [57]. However, the contact between magnesium hydride and the liquid electrolyte is unstable, often accompanied by the formation of an unstable SEI layer or irreversible side reactions. Therefore, an efficient strategy to reduce side reactions is the introduction of relatively stable solid-state electrolytes (SSE) [1,58–62].

Compare with liquid electrolytes, $LiBH_4$, as a solid-state electrolyte, has been demonstrated an appropriate electrochemical window (0–2.5 V) and a high lithium ionic conductivity (10^{-3} S cm^{-1}) at 390 K [63,64]. The MgH_2–$LiBH_4$ composite is well-known as a hydrogen storage material. A superior hydrogen exchange effect between MgH_2 and $LiBH_4$ has been reported previously [65], indicating the stability of the mixture when these materials are used as a negative electrode in LIBs. Therefore, inspired by both the superiorities of MgH_2@graphene as an electrode and $LiBH_4$ as an electrolyte, it would accelerate the conversion reaction and lead to a stable coulombic efficiency, a high specific capacity, and a favorable rate performance. In this work, we systematically investigate MgH_2 nanoparticles as an anode combined with SSE($LiBH_4$) for all-solid-state lithium-ion batteries (ASSLIBs). Introducing MgH_2 nanoparticles (MH^{nano})/MgH_2 nanoparticles on graphene (GMH^{nano}) is an effective way to ease its expansion and pulverization, and improve coulombic efficiency with cycle performance. We also focus on the origin of the voltage hysteresis in the conversion of MgH_2 after nano-crystallization and deduce insight into the mechanism of lithium-ion diffusion during the charge/discharge process.

2. Experimental method

2.1. Material preparation

All the starting materials were purchased from Sigma-Aldrich and used as received. These samples were handled in the purified argon gas-filled glove box (MIKROUNA) to avoid oxidation and water contamination. MgH_2 nanoparticles and MgH_2 nanoparticles on graphene (GR) with a loading ratio of 60 wt% were synthesized in-situ via the hydrogenation of dibutyl magnesium ($MgBu_2$) in cyclohexane (C_6H_{12}) as the previous report. Prior to being used as a solid-state electrolyte and an electric conductive agent, the commercial $LiBH_4$ and Ketjen Black were heated to 150 °C under a vacuum for 10 h to remove adsorbed water and impurities. The working electrode was prepared by ball-milling MgH_2, $LiBH_4$, and conductive carbon (Ketjen black) in a weight ratio of 25:25:50 with no further optimization. To prepare the full cell, the cathode composite consisted of Li_2S, $LiBH_4$, and Ketjen black with a weight ratio of 25: 25: 50.

2.2. Material characterization

The structural characterization was conducted by powder X-ray diffraction (XRD) measurement (Cu *Kα* radiation) at room temperature. The sample for XRD was protected with Kapton, a polyimide film (Du Pont-Toray Co., Ltd.) to avoid oxygen and water contamination during measurement. The loading ratio of MgH_2 nanoparticles was measured by Thermogravimetry (TG, Netzsch STA 449 F3) at a heating rate of 5 °C min^{-1}. The morphology and structure were carried out by a transmission electron microscope (TEM, JEOL JEM-2011F, at an acceleration voltage of 200 kV).

2.3. Computational details

Density functional theory (DFT) calculations were carried out using a projector-augmented wave (PAW) method as implemented in the Vienna ab initio simulation package (VASP) [66–68]. A generalized gradient approximation (GGA) of the Perdew-Burke-Ernzerhof (PBE) functional was employed to describe the exchange-correlation interaction [69]. An energy cutoff of 500 eV and 4 × 2 × 1 k-points mesh were applied to all calculations. The DFT-D3 dispersion correction method of Grimme was used to account for van der Waals (VdW) interactions in the system [70]. To achieve the minimum lattice mismatch between each pair of phases, the supercell consists of 32 MgH_2 unit cells and 24 $LiBH_4$ unit cells. The vacuum layer is thick enough to avoid interference from the adjacent periodic structures.

To evaluate the interphase stability, the formation energy (E_f) was defined as the energy difference before and after forming the heterojunction.

$$E_f = \frac{E_{Total} - E_{MgH_2} - E_{LiBH_4}}{n} \quad (1)$$

where E_{Total} are the total energy of $LiBH_4$/MgH_2/Gr or $LiBH_4$/MgH_2 heterojunction. E_{LiBH_4} is the energy of $LiBH_4$. E_{MgH_2} is the energy of MgH_2 with or without graphene. n is the number of MgH_2 unit cells. Therefore, a lower value of E_f indicates a more stable heterostructure.

2.4. Electrochemical measurement

The working electrode was loaded into stainless steel die with a 15 mm inner diameter and pressed into a pellet with $LiBH_4$ as a solid-state electrolyte at 20 MPa. Then a lithium foil was placed on the electrolyte as the counter electrode. The 2032-coin cell assembly was carried out in an Ar-filled glovebox with concentrations of moisture and oxygen below 1 ppm. Cyclic voltammetry (CV) with a scan rate of 0.1 mV s^{-1} between 0.25 and 1.5 V (vs Li^+/Li) and electrochemical impedance spectroscopy (EIS) from 7 MHz to 1 Hz were measured by an electrochemical workstation (Biologic VMP-300) at 120 °C. The cycling performance and rate efficiency of half-cell were tested using the same workstation between 0.25 and 1.5 V (vs Li^+/Li) at the current densities of 100–2000 mA g^{-1} at 120 °C. The specific capacity was calculated based on the weight of active MgH_2 only.

Coin cells were cycled in the Potentiostatic intermittent titration technique (PITT) from 1.0 to 0.25 V using a 10 mV step size with a current cut-off of 2 mA g^{-1} (< C/1000) of active material. The diffusion coefficient, D was calculated by measuring the linear slope of the ln(I) vs time (t) at each voltage step according to the following equation:

$$D_{(Li^+)} = -\frac{d(\ln(I))}{dt}\frac{4L^2}{\pi^2} \quad (2)$$

where I is the current of the potential step, t is the time within the potential step, and L is the diffusion length. According to TEM images, we assume our samples are spherical particles. Then, the diffusion length is approximately the radius of the spherical particles.

3. Results and discussion

As shown in Fig. 1(a), a flow diagram illustrated the assembly and measurement of the full cell. MgH_2^{nano} was achieved in the same manner consistent with our previous report [56]. The XRD patterns of the MgH_2^{nano} showed clear MgH_2 peaks (Fig. S3(a)). The loading ratio of MH^{nano} on graphene was set at 60 wt.% and was determined to be about 59.2 wt% by thermogravimetric analysis, as shown in Fig. S3(b). The direct observation of MgH_2 nanoparticle size and distribution on graphene was performed by TEM investigations (Fig. 1(b, c)), which showed an average size of pure MH^{nano} and GMH^{nano} around 14 nm. The HRTEM image and corresponding fast Fourier transform (FFT) image are shown in Fig. 1(d). The distances of the lattice fringes corresponding to lattice d spacing of MgH_2 (200) and (220) are 0.2257 and 0.1594 nm,

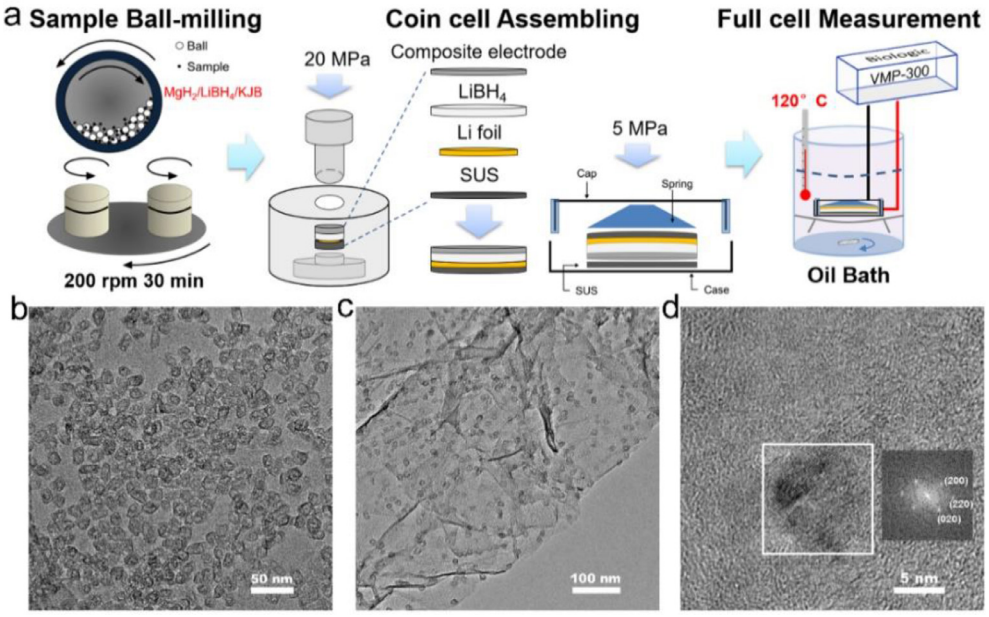

Fig. 1. (a) Schematic illustration of the assembly and measurement of full cell. Material characterization of GMH^{nano} and MH^{nano}. (b, c) Bright-field images of MH^{nano} and GMH^{nano}. (d) HRTEM images of GMH^{nano} and corresponding FFT image.

respectively. It was found that GMH^{nano} has a uniform dispersion and no obvious agglomeration, providing ample space for potential volume expansion. It also indicated a fast transport of lithium ions and easy diffusion at interphases during the discharging and charging processes. Meantime, graphene also provides strong support to prevent the active materials from falling off and leading to the inactivation of the system.

DFT calculations were also performed to investigate the interphase structure between $LiBH_4$ and MgH_2. For each phase, the most stable surface is considered first. Following the principles that the selected surface should be stoichiometric and no bonds should be broken, the (010) plane of $LiBH_4$ and the (110) plane of MgH_2 are cleaved and are used in all calculations [71,72]. Accordingly, the heterostructures of $LiBH_4/MgH_2$ in the presence and absence of graphene denoted as $LiBH_4/MgH_2$/Graphene and $LiBH_4/MgH_2$, are modeled as illustrated in Fig. 2(a, b), respectively. The formation energy (E_f) was calculated to evaluate the interphase stability. The computed E_f is –2.07 eV for the $LiBH_4/MgH_2$/Graphene system, and this value increases to –0.56 eV in $LiBH_4/MgH_2$ system. The much lower E_f of –2.07 eV indicates that the interface structure of $LiBH_4/MgH_2$/Gr is more stable. The electronic structures of these two systems were investigated to provide further insight. Fig. 2(c) demonstrates the charge redistribution of $LiBH_4/MgH_2$/Gr. Charge accumulation between $LiBH_4$ and MgH_2 suggests that the interphase interaction is robust, which is consistent with the favorable formation energy. The interaction between MgH_2 and graphene, as indicated by significant charge accumulation between Mg atoms and graphene, stabilizes the structure of MgH_2 and assures the strong interphase structure of $LiBH_4/MgH_2$/Gr. The projected density of states (PDOS) plotted in Fig. 2(d, e) also supports this conclusion as well. When combined with graphene, the H states and the Mg states become more delocalized, and they more obviously overlap the states of Li at ~ 4 and ~ –2 eV. Therefore, the cohesion between MgH_2 and $LiBH_4$ is enhanced with the help of graphene, which contributes to the good cycling stability that is observed experimentally.

The Pristine MH^{nano} composite material was used as the working electrode with the Li metal counter electrode to assemble half-cells. The half-cells were cycled at a constant current density of 100 mA g^{-1} (0.05 C) at 120 °C. The cutoff voltage was set to be 0.2–1.5 V (vs Li^+/Li) to avoid the Li–Mg alloying reaction ($Mg + xLi^+ + xe^- \rightleftharpoons MgLi_x$). Fig. 3(a) shows the galvanostatic dis/charge curves. It is observed that the MH^{nano}–Li cell showed an initial discharge capacity of 1030 mAh g^{-1} with a Coulombic efficiency of 86.8%. The first 20 cycles lead to the activation of the all-solid-state battery. Subsequently, the cycling performance remains stable. The cell still retains a discharge capacity of 650 mAh g^{-1} with a capacity retention of 61.8% after 50 cycles (Fig. 3(f)). Herein, differential curves based on the calculation of galvanostatic dis/charge curves are presented in Fig. 3(b). The first cycle of the discharging (charging) peak is located at ~ 0.30 V (0.72 V). The peak at 0.55 V is caused by the electrode activation and size effect of MH^{nano}, which disappears after 3 cycles. The conversion reaction peaks become symmetrical and move from 0.30 to 0.33 V after 20 cycles of activation. Furthermore, the peak observed at 0.72 V becomes broad and polarized to 0.78 V and is assigned to the reversible reaction of MgH_2. A large separation of the voltage on charge and discharge ($\Delta E = 0.45$ V) implies slow kinetics of the electrodes. The migration rate of lithium ions and electrons cannot satisfy the reaction rate of the active domains since the massive interfacial regions of MH^{nano} are derived from nano-crystallization. As the cycling progresses, the voltage polarization is slightly increased to 0.48 V (50th). Furthermore, a long-term cycling performance has been achieved as shown in Fig. S4(a). The reversible capacity retains 499 mAh g^{-1} at the 137th cycle (0.05 C), with a Coulombic efficiency close to 99.9%. However, the volume expansion and agglomeration of MH^{nano} further lead to a significant irreversible capacity and poor rate capability (Fig. 3(e)).

Fig. 3(c) presents the conversion behavior of a GMH^{nano} electrode in the galvanostatic dis/charge tests. According to the bright field image (Fig. 1(c)) and DFT calculations, no independent $MgH_2{}^{nano}$ could be found outside the graphene substrate, indicating a strong interaction and sustentation between $MgH_2{}^{nano}$ and graphene. An initial discharge capacity of 1959 mAh g^{-1} is obtained with a Coulombic efficiency of 72.4%, which is close to the theoretical capacity. Notably, a high reversible capacity of 1214 mAh g^{-1} with a Coulombic efficiency of 98.6% has been achieved after 50 cycles (Fig. 3(f)). Meantime, long-term cy-

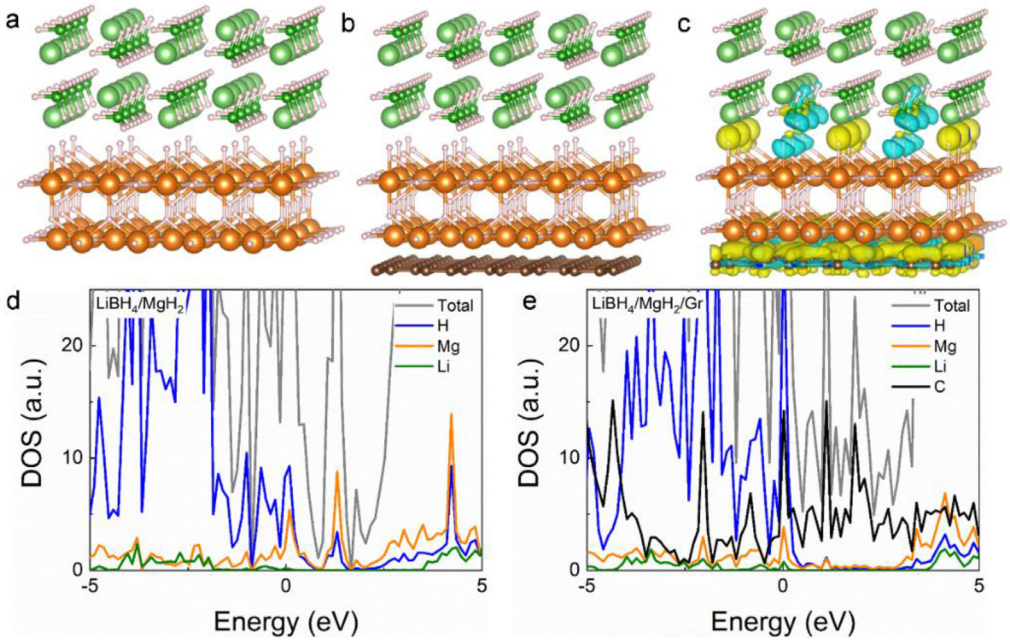

Fig. 2. Schematic illustrations of (a) $LiBH_4/MgH_2$ and (b) $LiBH_4/MgH_2$/Gr heterojunctions. (c) Charge density difference plot of $LiBH_4/MgH_2$/Gr. The C, Mg, Li, B, and H atoms are depicted in brown, orange, green, dark green, and white, respectively. Areas of charge accumulation are shown in yellow while depletion areas are shown in blue. PDOS of (d) $LiBH_4/MgH_2$ and (e) $LiBH_4/MgH_2$/Gr. The fermi level is aligned to zero.

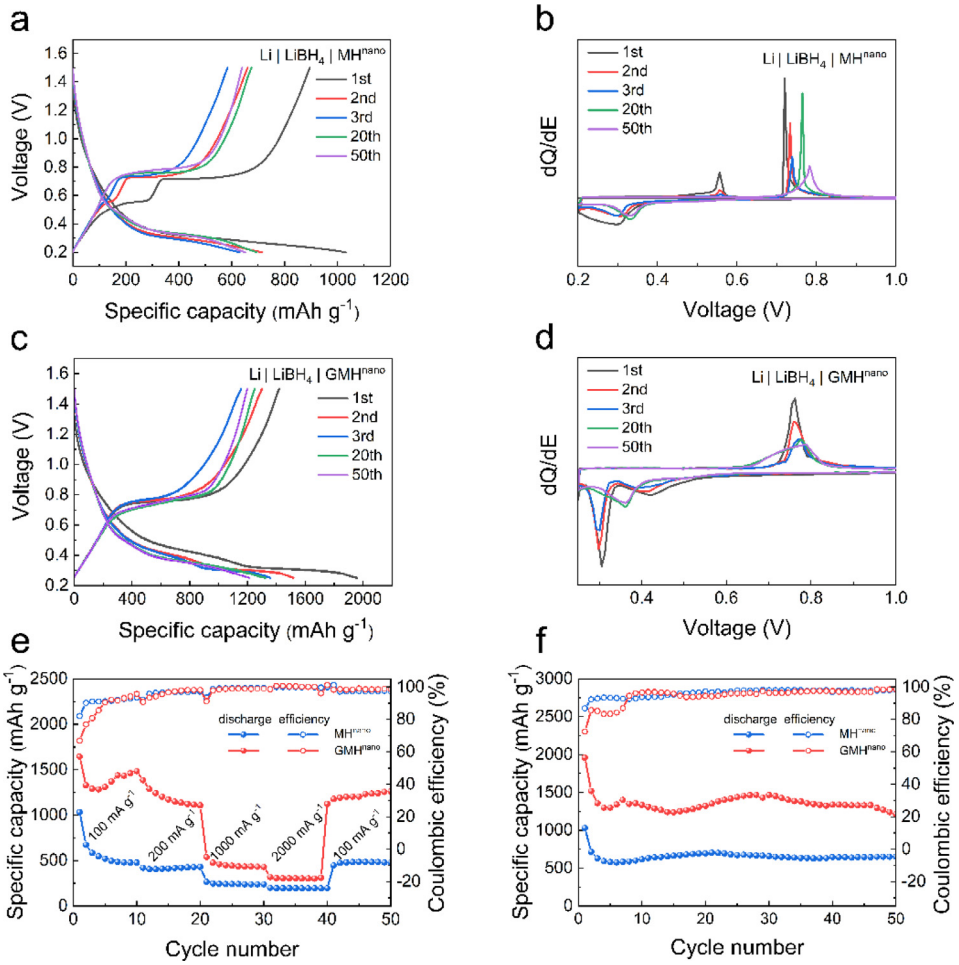

Fig. 3. Electrochemical performances. (a) Voltage profiles of MH^{nano}–Li cell. (b) The corresponding derivative curves (dQ/dE) of MH^{nano}–Li cell. (c) Voltage profiles of GMH^{nano}–Li cell. (d) The corresponding derivative curves (dQ/dE) of GMH^{nano}–Li cell. (e) Rate capacity of MH^{nano} and GMH^{nano} electrodes at various current densities from 100 to 2000 mA g^{-1}, respectively. (f) Cycling performances and Coulombic efficiency of MH^{nano} and GMH^{nano} electrodes at a current density of 100 mA g^{-1}.

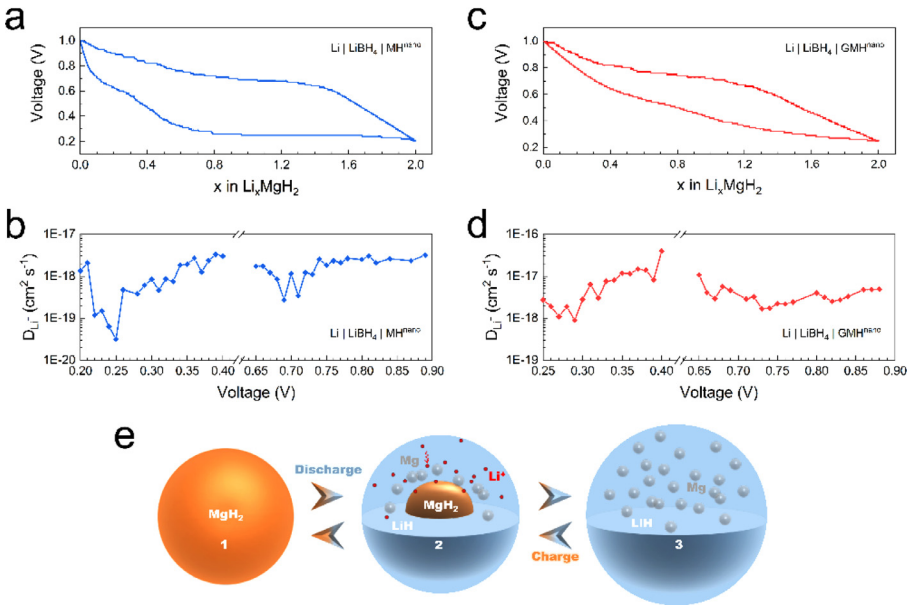

Fig. 4. Diffusion coefficient of MH^{nano} (a, b) and GMH^{nano} (c, d) extracted from high-resolution PITT characterization. (e) Proposed lithiation/delithiation behavior of MgH_2 nanoparticle.

cling was performed (Fig. S4(b)). The reversible capacity retains 597 mAh g^{-1} (400 mA g^{-1}) at 200 cycles, with a Coulombic efficiency close to 99.9%. Fig. 3(d) presents the differential curves according to the corresponding voltage profiles. After 20 cycles of activation, both the reduction peak (0.36 V) and oxidation peak (0.75 V) become symmetrical, indicating a good Coulombic efficiency and reversible capacity. Furthermore, the average discharge specific capacities of different current densities are 1404 mAh g^{-1} (100 mA g^{-1}), 1192 mAh g^{-1} (200 mA g^{-1}), 452 mAh g^{-1} (1000 mA g^{-1}), and 305 mAh g^{-1} (2000 mA g^{-1}), respectively (Fig. 3(e)). The specific capacity of the cell is 1200 mAh g^{-1} (100 mA g^{-1}), and the Coulombic efficiency is over 97% after high current density cycling. No Li-Mg alloy phase is observed after long-term cycling from the XRD patterns (Fig. S5). Compared with commercial MgH_2 and MH^{nano}, self-assembled GMH^{nano} has superior performance in terms of specific capacity, cycle stability, and rate performance.

Accurate characterization of potential polarization is important in understanding the electrode kinetics and reaction pathways of conversion materials. However, galvanostatic intermittent titration techniques (GITT) are suitable for intercalation materials, but not for conversion materials. PITT is a helpful method for studying the diffusion coefficient of Li^+ ions. More specifically, the conversion reaction, consisting of many small plateaus (Fig. 4(a, c)), can be attributed to compositional changes with new phases forming from conversions (Fig. 4(b, d)). The small region of Cottrellian behavior observed in PITT curves can be ascribed to a localized range of solid solution reactions, occurring at a very small voltage scale where the interface moves forward, and thus is fundamentally dependent on diffusion processes (Fig. 4(e)) [73,74]. The lithiation/delithiation behavior of the MH^{nano} sample is similar to that of GMH^{nano}. Furthermore, it was found that MH^{nano} had a diffusion rate of 3.16×10^{-20} cm^2 s^{-1} at 0.25 V and 2.73×10^{-19} cm^2 s^{-1} at 0.69 V, respectively. By contrast, larger values of $D_{(Li^+)}$ for GMH^{nano} (8.92×10^{-19} cm^2 s^{-1} at 0.29 V and 1.69×10^{-18} cm^2 s^{-1} at 0.73 V) were obtained. Importantly, the diffusion coefficients of GMH^{nano} were one or two orders higher than that of MH^{nano}. It is understandable that better kinetics of lithium ion migration and reaction are due to the graphene support. In general, all coefficients are quite low, which implies a slow diffusion process and reflects the intrinsic voltage hysteresis.

From the practical perspective, a further attempt of all solid-state full cells was investigated by matching them with the commercial Li_2S cathode. Fig. 5 shows the cycle performance of the full cell (GMH^{nano}|$LiBH_4$|Li_2S) at 100 mA g^{-1} for MgH_2. The cathode composite has a molar ratio of 30% higher than the metal hydride anode to compensate for the lowest capacity of the former compared to the anode. In order to evaluate the performance of the GMH^{nano} composite, the capacity of the full cell was expressed per g of active material in anode material. As the galvanostatic discharge curves (GMH^{nano}) and charge (Li_2S) curves shown in Fig. 5(a, b), the main charge plateau is range from 1.8 to 2.2 V, which is equal to the potential difference between the GMH^{nano} anode (lithiation 0.5 to 0.2 V), and Li_2S cathode (delithiation 2.3 to 2.5 V). In contrast, suffering from extremely poor electronic/ionic conductivity, the Li_2S cathode as an insulator requires a high overpotential for activation in its first cycle [75–78]. As a result, the main discharge plateau consists of two parts owing to the two discharge platforms of Li_2S (lithiation 2.2 to 2.0 V and 1.4 to 1.2 V). The reversible specific capacity reaches 2087 mAh g^{-1} for the first cycle, which suggests the complete lithiation of the MgH_2. It decreases to 1268 mAh g^{-1} for the fifth cycle with a coulombic efficiency of close to 97% (Fig. 5(c)). The battery capacity decline can be explained by the inactivation of lithium sulfide occurring on the cathode side [79,80]. The second discharge platform would fade away due to the pulverization of lithium sulfide particles during cycles [81–83]. The above attempts of the full cell indicate that practical applications of hydrides still require further improvement on the cathode side [76,78,82,83].

Overall, the electrochemical properties of the GMH^{nano} electrode exhibit better performance than those of MH^{nano}, commercial MH (Table S1). However, conversion electrodes exhibit larger polarization after nano-crystallization, which is distinct from the behavior of intercalation electrodes. The migration rate of lithium ions to the interfacial regions of MH^{nano} cannot match the rate of lithium-ion consumption with active domains [2,71]. On the other hand, as opposed to lithium insertion/extraction, which relies exclusively on the mobility of Li^+, the conversion reaction requires

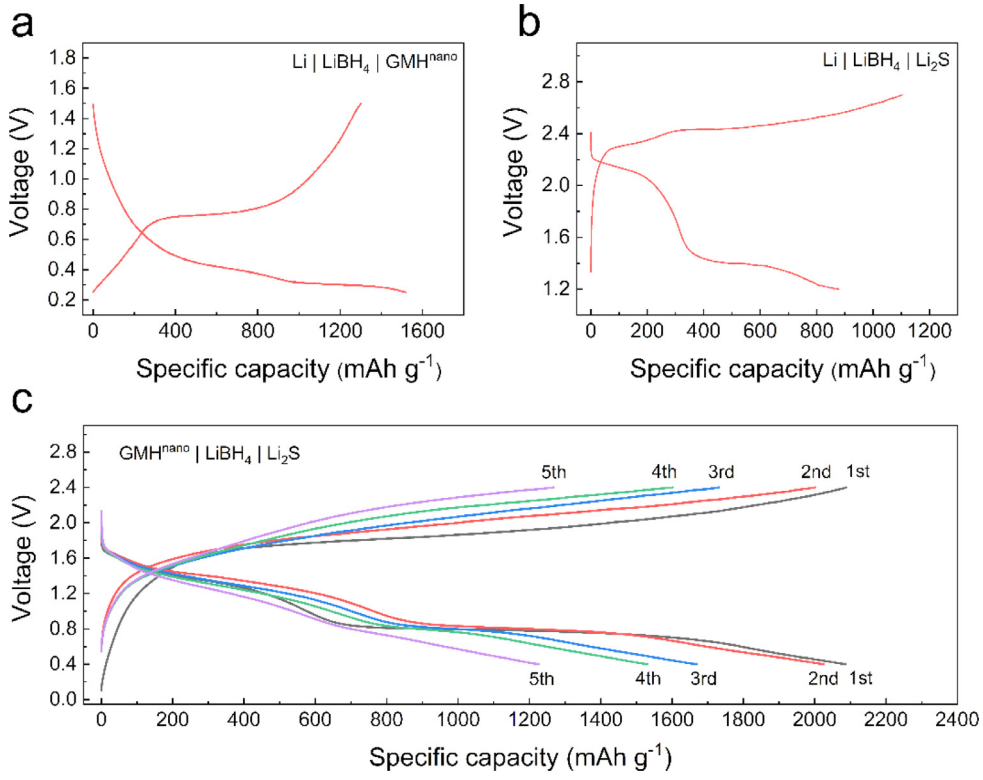

Fig. 5. Voltage profile of the GMH^{nano} (a) and Li_2S (b) half-cells at 0.05C and 120 °C. (c) Charge/discharge profiles of the first five cycles at 0.05 C of the $GMH^{nano}/LiBH_4/Li_2S$ full-cell.

consideration of other ions, such as Mg^+ and H^-, which should not be simply assigned to Li^+.

4. Conclusions

In summary, GMH^{nano} shows a reversible capacity of 1214 mAh g^{-1} after 50 cycles. The as-prepared electrodes deliver a good rate capability of 305 mAh g^{-1} even at a high current density of 2000 mA g^{-1}. Significantly enhanced cycle life with a notable capacity of 597 mAh g^{-1} (0.2 C) is obtained even after 200 cycles. Such a result, owing to the strong nanoparticle-graphene interactions, not only improves the lithium-ion reaction rate, but also increases the charge transfer rate, and finally effectively enhances the lithium storage capacity. Besides, the full cell measurement also shows a great utilization potential in all-solid-state lithium-ion batteries. Further development on the cathode and anode materials will be studied to obtain the overall high performance of the full cell.

Declaration of Competing Interest

The authors declare that they have no known competing financial interests or personal relationships that could have appeared to influence the work reported in this paper.

Acknowledgments

This study was financially supported by the National Natural Science Foundation of China (Nos. 52171180, 51802154, and 51971065), the National Science Fund for Distinguished Young Scholars (No. 51625102), the Innovation Program of Shanghai Municipal Education Commission (No. 2019–01–07–00–07-E00028), the Fundamental Research Funds for the Central Universities (No. NG2022005), the Scientific and Technological Innovation Special Fund for Carbon Peak and Carbon Neutrality of Jiangsu Province (No. BK20220039), and the Open Fund for Graduate Innovation Base in Nanjing University of Aeronautics and Astronautics (No. xcxjh20210612).

Supplementary materials

Supplementary material associated with this article can be found, in the online version, at doi:10.1016/j.jmst.2023.01.028.

References

[1] A. Manthiram, X.W. Yu, S.F. Wang, Nat. Rev. Mater. 2 (2017) 16103.
[2] P.G. Bruce, B. Scrosati, J.-.M. Tarascon, Angew. Chem., Int. Ed. 47 (2008) 2930–2946.
[3] T.F. Zhang, W.J. He, W. Zhang, T. Wang, P. Li, Z.M. Sun, X.B. Yu, Chem. Sci. 11 (2020) 8686–8707.
[4] A. Manthiram, ACS Cent. Sci. 3 (2017) 1063–1069.
[5] F.Q. Lu, Y.P. Pang, M.F. Zhu, F.D. Han, J.H. Yang, F. Fang, D.L. Sun, S.Y. Zheng, C.S. Wang, Adv. Funct. Mater. 29 (2019) 1809219.
[6] Q. Li, L.S. Han, Q. Luo, X.Y. Liu, J. Yi, Batter. Supercaps 5 (2022) e202100417.
[7] R.T. Li, Y.X. Du, Y.H. Li, Z.X. He, L. Dai, L. Wang, X.W. Wu, J.J. Zhang, J. Yi, ACS Energy Lett. 8 (2022) 457–476.
[8] K. Wu, F.H. Ning, J. Yi, X.Y. Liu, J.Q. Qin, Y.Y. Liu, J.J. Zhang, J. Energy Chem. 69 (2022) 237–243.
[9] X.Y. Liu, Y.Z. Fang, P.C. Liang, J.H. Xu, B. Xing, K. Zhu, Y.Y. Liu, J.J. Zhang, J. Yi, Chin. Chem. Lett. 32 (2021) 2899–2903.
[10] B. Anasori, M.R. Lukatskaya, Y. Gogotsi, Nat. Rev. Mater. 2 (2017) 16098.
[11] I.H. Son, J. Hwan Park, S. Kwon, S. Park, M.H. Rümmeli, A. Bachmatiuk, H.J. Song, J. Ku, J.W. Choi, J. Choi, S.-.G. Doo, H. Chang, Nat. Commun. 6 (2015) 7393.
[12] M. Naguib, J. Halim, J. Lu, K.M. Cook, L. Hultman, Y. Gogotsi, M.W. Barsoum, J. Am. Chem. Soc. 135 (2013) 15966–15969.
[13] J.M. Jiang, J.R. Yuan, P. Nie, Q. Zhu, C.L. Chen, W.J. He, T.F. Zhang, H. Dou, X.G. Zhang, J. Mater. Chem. A 8 (2020) 3956–3966.
[14] Y. Sun, J.J. Xue, S.Y. Dong, Y.D. Zhang, Y.F. An, B. Ding, T.F. Zhang, H. Dou, X.G. Zhang, J. Mater. Sci. 55 (2020) 5166–5176.
[15] H.-.W. Li, M. Zhu, C. Buckley, T.R. Jensen, Inorganics 6 (2018) 91.
[16] Y. Oumellal, A. Rougier, G.A. Nazri, J.-.M. Tarascon, L. Aymard, Nat. Mater. 7 (2008) 916–921.

[17] G.L. Xia, Y.B. Tan, X.W. Chen, D.L. Sun, Z.P. Guo, H.K. Liu, L.Z. Ouyang, M. Zhu, X.B. Yu, Adv. Mater. 27 (2015) 5981–5988.
[18] S. Sartori, F. Cuevas, M. Latroche, Appl. Phys. A-Mater. Sci. Process. 122 (2016) 1–7.
[19] S.L. Zhong, S.L. Ju, Y.F. Shao, W. Chen, T.F. Zhang, Y.Q. Huang, H.Y. Zhang, G.L. Xia, X.B. Yu, J. Energy Chem. 62 (2021) 431–439.
[20] M. Guo, S.L. Zhong, T. Xu, Y.Q. Huang, G.L. Xia, T.F. Zhang, X.B. Yu, J. Mater. Chem. A 9 (2021) 23841–23849.
[21] Y. Jin, B. Zhu, Z.D. Lu, N. Liu, J. Zhu, Adv. Energy Mater. 7 (2017) 1700715.
[22] Q. Xu, J.-.Y. Li, J.-.K. Sun, Y.-.X. Yin, L.-.J. Wan, Y.-.G. Guo, Adv. Energy Mater. 7 (2017) 1601481.
[23] J. Liu, Q. Zhang, T. Zhang, J.-.T. Li, L. Huang, S.-.G. Sun, Adv. Funct. Mater. 25 (2015) 3599–3605.
[24] W.J. He, T.F. Zhang, Z.W. Li, J.M. Jiang, C.L. Chen, N. Liu, H. Dou, X.G. Zhang, J. Mater. 7 (2021) 802–809.
[25] W.J. He, T.F. Zhang, J.M. Jiang, C.L. Chen, Y.D. Zhang, N. Liu, H. Dou, X.G. Zhang, ACS Appl. Energy Mater. 3 (2020) 4394–4402.
[26] S.Y. Bai, X.Z. Liu, K. Zhu, S.C. Wu, H.S. Zhou, Nat. Energy 1 (2016) 16094.
[27] Q. Pang, X. Liang, C.Y. Kwok, L.F. Nazar, Nat. Energy 1 (2016) 16132.
[28] Z.W. Seh, Y.M. Sun, Q.F. Zhang, Y. Cui, Chem. Soc. Rev. 45 (2016) 5605–5634.
[29] Y. Lu, L. Yu, X.W. (David) Lou, Chem 4 (2018) 972–996.
[30] Q.B. Xia, W.J. Li, Z.C. Miao, S.L. Chou, H.K. Liu, Nano Res. 10 (2017) 4055–4081.
[31] W. Liu, P. Oh, X. Liu, M.-.J. Lee, W. Cho, S. Chae, Y. Kim, J. Cho, Angew. Chem., Int. Ed. 54 (2015) 4440–4457.
[32] Y. Zhao, X.F. Li, B. Yan, D.B. Xiong, D.J. Li, S. Lawes, X.L. Sun, Adv. Energy Mater. 6 (2016) 1502175.
[33] M.B. Zheng, H. Tang, L.L. Li, Q. Hu, L. Zhang, H.G. Xue, H. Pang, Adv. Sci. 5 (2018) 1700592.
[34] W.Z. Wang, Q. Zhang, T. Jiang, S.J. Li, J.Z. Gao, X.H. Liu, C.F. Lin, Adv. Energy Mater. 12 (2022) 2200656.
[35] R.J. Li, G.S. Liang, X.Z. Zhu, Q.F. Fu, Y.J. Chen, L.J. Luo, C.F. Lin, Energy Environ. Mater. 4 (2021) 65–71.
[36] S.Y. Ma, T. Jiang, J.B. Deng, Q. Zhang, Y.J. Ou, X.H. Liu, C.F. Lin, K.K. Wang, X.S. Zhao, Energy Storage Mater. 46 (2022) 366–373.
[37] Q. Zhang, S.Y. Ma, W.Z. Wang, S.F. Gao, Y.J. Ou, S.J. Li, X.H. Liu, C.F. Lin, Energy Storage Mater. 52 (2022) 637–645.
[38] Y.Y. Zhu, L.Z. Ouyang, H. Zhong, J.W. Liu, H. Wang, H.Y. Shao, Z.G. Huang, M. Zhu, Angew. Chem., Int. Ed. 59 (2020) 8623–8629.
[39] L.Z. Ouyang, W. Chen, J.W. Liu, M. Felderhoff, H. Wang, M. Zhu, Adv. Energy Mater. 7 (2017) 1700299.
[40] Q. Luo, Y.L. Guo, B. Liu, Y.J. Feng, J.Y. Zhang, Q. Li, K.C. Chou, J. Mater. Sci. Technol. 44 (2020) 171–190.
[41] Q. Li, Q. Lin, K.C. Chou, L.J. Jiang, J. Mater. Sci. 39 (2004) 61–65.
[42] Y.O. Ma, T.F. Zhang, W.J. He, Q. Luo, Z.W. Li, W. Zhang, J.P. He, Q. Li, Int. J. Hydrogen Energy 45 (2020) 12048–12070.
[43] L.Z. Ouyang, Z.J. Cao, H. Wang, J.W. Liu, D.L. Sun, Q.A. Zhang, M. Zhu, Int. J. Hydrogen Energy 38 (2013) 8881–8887.
[44] Q.H. Cheng, D.L. Sun, X.B. Yu, J. Alloy. Compd. 769 (2018) 167–185.
[45] B.P. Zhang, Y.S. Si, Q.F. Gu, M. Chen, X.B. Yu, ACS Appl. Mater. Interfaces 11 (2019) 28987–28995.
[46] J. Cuan, Y. Zhou, T.F. Zhou, S.G. Ling, K. Rui, Z.P. Guo, H.K. Liu, X.B. Yu, Adv. Mater. 31 (2019) 1803533.
[47] A. Inoishi, H. Sato, Y.X. Chen, H. Saito, R. Sakamoto, H. Sakaebe, S. Okada, RSC Adv. 12 (2022) 10749–10754.
[48] F. Cano-Banda, A. Gallardo-Gutierrez, L. Luviano-Ortiz, A. Hernandez-Guerrero, A. Jain, T. Ichikawa, Int. J. Hydrogen Energy 46 (2020) 1030–1037.
[49] Q. Li, Y.F. Lu, Q. Luo, X.H. Yang, Y. Yang, J. Tan, Z.H. Dong, J. Dang, J.B. Li, Y. Chen, B. Jiang, S.H. Sun, F.S. Pan, J. Magn. Alloy. 9 (2021) 1922–1941.
[50] H.W. Song, J. Su, C.X. Wang, Adv. Energy Mater. 9 (2019) 1900426.
[51] J. Su, H.W. Song, C.X. Wang, Adv. Funct. Mater. 29 (2019) 1907154.
[52] H.W. Song, J. Su, C.X. Wang, ACS Appl. Mater. Interfaces 11 (2019) 37867–37874.
[53] R. Hu, Y.Z. Fang, X.Y. Liu, K. Zhu, D.X. Cao, J. Yi, G.L. Wang, Chem. Res. Chin. Univ. 37 (2021) 311–317.
[54] H. Wang, H.J. Lin, W.T. Cai, L.Z. Ouyang, M. Zhu, J. Alloy. Compd. 658 (2016) 280–300.
[55] Y. Oumellal, C. Zlotea, S. Bastide, C. Cachet-Vivier, E. Léonel, S. Sengmany, E. Leroy, L. Aymard, J.-.P. Bonnet, M. Latroche, Nanoscale 6 (2014) 14459–14466.
[56] B.P. Zhang, G.L. Xia, D.L. Sun, F. Fang, X.B. Yu, ACS Nano 12 (2018) 3816–3824.
[57] G.L. Xia, B.P. Zhang, X.W. Chen, D.L. Sun, Z.P. Guo, F.X. Liang, W.D. Zou, Z.Z. Yang, X.B. Yu, ACS Nano 12 (2018) 8177–8186.
[58] B.Y. Liu, Y.H. Gong, K. Fu, X.G. Han, Y.G. Yao, G. Pastel, C.P. Yang, H. Xie, E.D. Wachsman, L.B. Hu, ACS Appl. Mater. Interfaces 9 (2017) 18809–18815.
[59] T.F. Zhang, Y.M. Wang, T. Song, H. Miyaoka, K. Shinzato, H. Miyaoka, T. Ichikawa, S.Q. Shi, X.G. Zhang, S. Isobe, N. Hashimoto, Y. Kojima, Joule 2 (2018) 1522–1533.
[60] A. Unemoto, T. Ikeshoji, S. Yasaku, M. Matsuo, V. Stavila, T.J. Udovic, S. Orimo, Chem. Mater. 27 (2015) 5407–5416.
[61] S. Kim, N. Toyama, H. Oguchi, T. Sato, S. Takagi, T. Ikeshoji, S.I. Orimo, Chem. Mater. 30 (2018) 386–391.
[62] K. Wu, J. Yi, X.Y. Liu, Y. Sun, J. Cui, Y.H. Xie, Y.Y. Liu, Y.Y. Xia, J.J. Zhang, Nano-Micro Lett. 13 (2021) 1–11.
[63] M. Matsuo, Y. Nakamori, S.I. Orimo, H. Maekawa, H. Takamura, Appl. Phys. Lett. 91 (2007) 224103.
[64] S. Kim, H. Oguchi, N. Toyama, T. Sato, S. Takagi, T. Otomo, D. Arunkumar, N. Kuwata, J. Kawamura, S. Orimo, Nat. Commun. 10 (2019) 1081.
[65] L. Zeng, H. Miyaoka, T. Ichikawa, Y. Kojima, J. Phys. Chem. C 114 (2010) 13132–13135.
[66] G. Kresse, J. Furthmüller, Phys. Rev. B 54 (1996) 11169–11186.
[67] G. Kresse, J. Hafner, Phys. Rev. B 47 (1993) 558–561.
[68] P.E. Blöchl, Phys. Rev. B 50 (1994) 17953–17979.
[69] J.P. Perdew, K. Burke, M. Ernzerhof, Phys. Rev. Lett. 77 (1996) 3865–3868.
[70] H.T. Larijani, M. Jahanshahi, M.D. Ganji, M.H. Kiani, Phys. Chem. Chem. Phys. 19 (2017) 1896–1908.
[71] D. Meggiolaro, G. Gigli, A. Paolone, P. Reale, M.L. Doublet, S. Brutti, J. Phys. Chem. C 119 (2015) 17044–17052.
[72] N.D. Lepley, N.A.W. Holzwarth, Y.A. Du, Phys. Rev. B 88 (2013) 104103.
[73] J.K. Ko, K.M. Wiaderek, N. Pereira, T.L. Kinnibrugh, J.R. Kim, P.J. Chupas, K.W. Chapman, G.G. Amatucci, ACS Appl. Mater. Interfaces 6 (2014) 10858–10869.
[74] M.D. Levi, E. Markevich, D. Aurbach, Electrochim. Acta 51 (2005) 98–110.
[75] J.Y. Hwang, S. Shin, C.S. Yoon, Y.K. Sun, ACS Energy Lett. 4 (2019) 2787–2795.
[76] G.Q. Tan, R. Xu, Z.Y. Xing, Y.F. Yuan, J. Lu, J.G. Wen, C. Liu, L. Ma, C. Zhan, Q. Liu, T.P. Wu, Z.L. Jian, R. Shahbazian-Yassar, Y. Ren, D.J. Miller, L.A. Curtiss, X.L. Ji, K. Amine, Nat. Energy 2 (2017) 1–10.
[77] S.Y. Zheng, Y. Chen, Y.H. Xu, F. Yi, Y.J. Zhu, Y.H. Liu, J.H. Yang, C.S. Wang, ACS Nano 7 (2013) 10995–11003.
[78] S.Q. Li, D. Leng, W.Y. Li, L. Qie, Z.H. Dong, Z.Q. Cheng, Z.Y. Fan, Energy Storage Mater. 27 (2020) 279–296.
[79] M.L. Yu, S. Zhou, Z.Y. Wang, W. Pei, X.J. Liu, C. Liu, C.L. Yan, X.Y. Meng, S. Wang, J.J. Zhao, J.S. Qiu, Adv. Funct. Mater. 29 (2019) 1–11.
[80] Y.Z. Liu, X.Y. Meng, Z.Y. Wang, J.S. Qiu, Sci. Adv. 8 (2022) 8390.
[81] Z.H. Liu, T.F. Zhang, S.L. Ju, Y.D. Ji, Z.T. Hu, Y.T. Lv, G.L. Xia, X.B. Yu, ACS Appl. Energy Mater. 5 (2022) 14301–14310.
[82] F.X. Wu, A. Magasinski, G. Yushin, J. Mater. Chem. A 2 (2014) 6064–6070.
[83] J.R. He, Y.F. Chen, W.Q. Lv, K.C. Wen, C. Xu, W.L. Zhang, Y.R. Li, W. Qin, W.D. He, ACS Nano 10 (2016) 10981–10987.